Article

Free Radicals Generated in Perfluorocarbon−Water (Liquid−Liquid) Interfacial Contact Electrification and Their Application in Cancer Therapy

Haimei Li, Zichen Wang, Xu Chu, Yi Zhao, Guangqin He, Yulin Hu, Yi Liu,* Zhong Lin Wang,* and Peng Jiang*

ACCESS | 📊 Metrics & More | 📖 Article Recommendations | 🆂🅸 Supporting Information

ABSTRACT: Electron transfer during solid−liquid contact electrification has been demonstrated to produce reactive oxygen species (ROS) such as hydroxyl radicals ($^{\bullet}OH$) and superoxide anion radicals ($^{\bullet}O_2^-$). Here, we show that such a process also occurs in liquid−liquid contact electrification. By preparing perfluorocarbon nanoemulsions to construct a perfluorocarbon−water "liquid−liquid" interface, we confirmed that electrons were transferred from water to perfluorocarbon in ultrasonication-induced high-frequency liquid−liquid contact to produce $^{\bullet}OH$ and $^{\bullet}O_2^-$. The produced ROS could be applied to ablate tumors by triggering large-scale immunogenic cell death in tumor cells, promoting dendritic cell maturation and macrophage polarization, ultimately activating T cell-mediated antitumor immune response. Importantly, the raw material for producing $^{\bullet}OH$ is water, so the tumor therapy is not limited by the endogenous substances (O_2, H_2O_2, etc.) in the tumor microenvironment. This work provides new perspectives for elucidating the mechanism of generation of free radicals in liquid−liquid contact and provides an excellent tumor therapeutic modality.
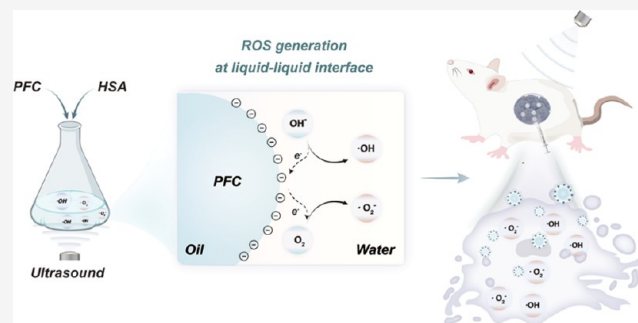
INTRODUCTION

Contact electrification is a ubiquitous physical phenomenon in nature. Our recent work indicates that electron transfer is the main mechanism of contact electrification between solid−solid interfaces.[1−3] Subsequently, electron transfer during solid−liquid contact electrification is also confirmed,[4−6] and a two-step model ("Wang model") has been proposed for the formation of a solid−liquid electric double layer: In the first step, the collision between two atoms of the solid and liquid phases causes electron transfer due to the overlap of electron clouds, making the solid surface negatively charged. In the second step triggered immediately afterward, the negative charge on the solid surface adsorbs the opposite charge in the liquid due to the presence of electrostatic attraction, thereby forming an electric double layer.[5,7−9] More importantly, the electron transfer in the solid−liquid contact can lead to redox reactions at the interface, producing reactive oxygen species (ROS). Wang et al. found that both hydroxyl radicals ($^{\bullet}OH$) and superoxide anion radicals ($^{\bullet}O_2^-$) were generated in the ultrasonication-induced high-frequency solid−liquid contact between fluorinated ethylene propylene (FEP) and aqueous media.[10,11] Considering the possible interference of ultrasonication on the electron-transfer process, Jiang et al. developed a highly sensitive strategy based on a long capillary tube to directly investigate the electron transfer and free radical
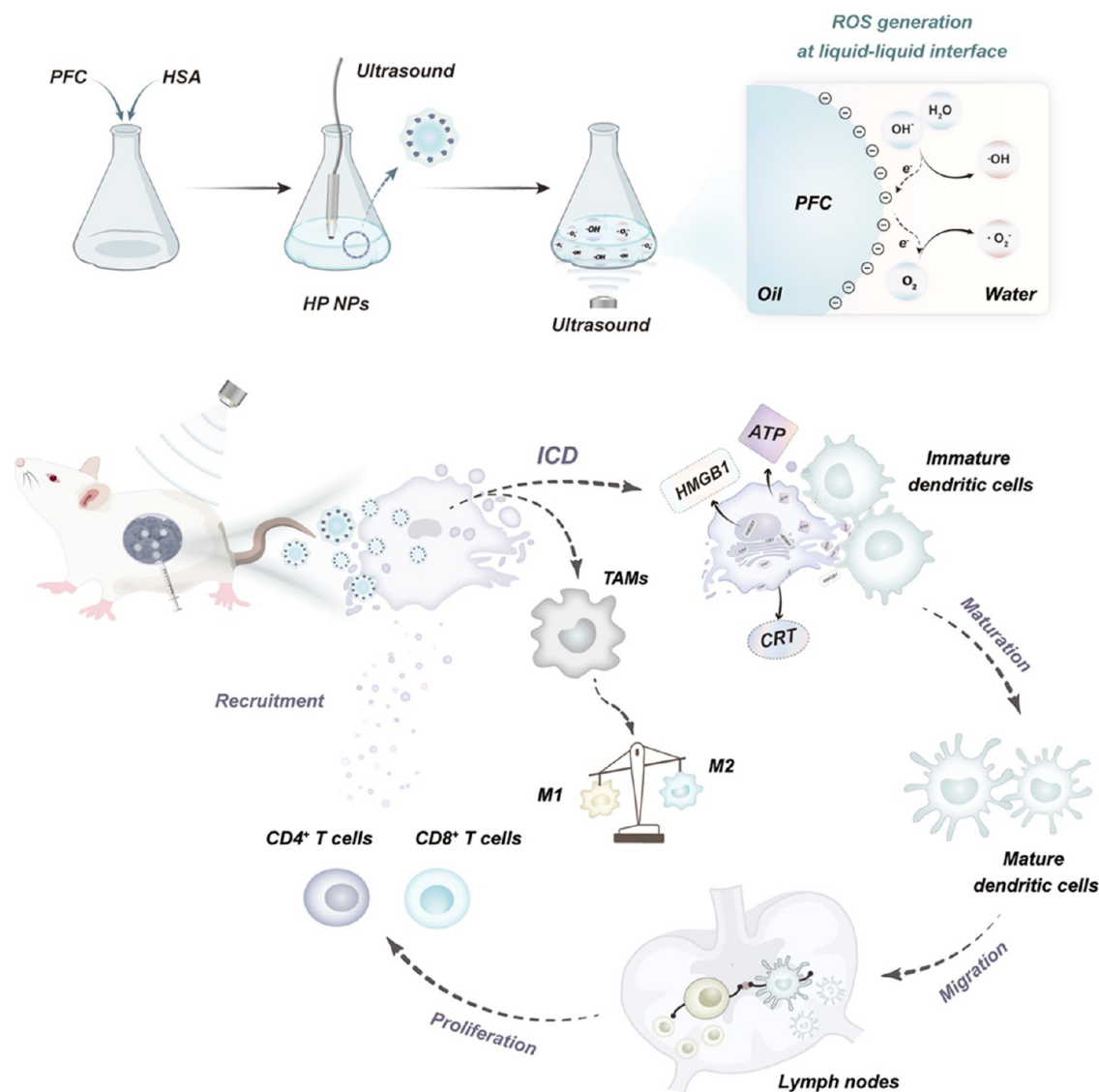
generation during solid−liquid contact without the assistance of ultrasonication. In that study, a small droplet was pushed by N_2 gas to flow through long polytetrafluoroethylene (PTFE) capillaries, providing a continuous solid−liquid contact for the droplet. Surprisingly, $^{\bullet}OH$ was successfully detected in the PTFE-treated droplets, which directly proves that electron transfer occurred in solid−liquid contact and induced redox reactions at the interface, producing sufficiently high concentrations of free radicals in small droplets.[12] Interestingly, $^{\bullet}O_2^-$ was not detected in the PTFE-treated droplets without the assistance of ultrasonication. These studies illustrate the importance of electron transfer during contact electrification because many important processes in biology, chemistry, and physics take place at interfaces rather than in homogeneous solutions. For instance, enzyme reactions both in nature and technical applications commonly occur at the interface of immiscible phases.[13] In chemistry, many reactions require

Scheme 1. Schematic Illustration of the Preparation of HP NPs, ROS Generation in Liquid−Liquid Contact, and ROS-Induced ICD-Mediated Immune Recruitment and Adaptive Immune Response

interfacial catalysis to occur at the interface of water−organic emulsions.[14]

Although the mechanism of electron transfer during solid−liquid contact electrification has been clearly elucidated, it still remains to be further investigated in the liquid−liquid case. Moreover, the potential applications of free radicals based on the contact electrification mechanism still remain to be explored.[10,15,16] Numerous studies have demonstrated that ROS plays key roles in tumor treatment, including sonodynamic therapy (SDT), chemodynamic therapy (CDT), photodynamic therapy (PDT), etc.[17−19] However, the efficacy of these ROS-mediated anticancer therapies is limited by the endogenous substances in the tumor microenvironment. In the cases of SDT and PDT, the anticancer efficacy is limited by the hypoxic tumor microenvironment,[20,21] and the CDT efficacy relies on H_2O_2, which produces •OH via the Fenton reaction.[22,23] Since the raw material for producing •OH by electron transfer from interfacial contact is water, which is abundant in the body, the free radical generation based on the liquid−liquid contact is expected to be a promising solution to construct effective anticancer therapeutic

modalities that are not restricted by endogenous substances in the tumor microenvironment.

Herein, perfluorocarbon (PFC) nanoemulsions were prepared to construct the perfluorocarbon−water interface to investigate electron transfer during the liquid−liquid contact (Scheme 1). To increase the water solubility and stability, the nanoemulsions were modified by human serum albumin (HSA). High-frequency liquid−liquid contact separation between water and PFC nanoemulsions is achieved by the generation and rupture of cavitation bubbles during ultrasonic oscillation. We demonstrated that electrons can be transferred from H_2O and hydroxide ions (OH^-) to perfluorocarbon in ultrasonication-induced high-frequency liquid−liquid contact to produce •OH. In addition, O_2 in water can gain electrons from negatively charged PFC (PFC*) to produce $•O_2^-$. Based on this ROS generation mechanism, the HSA-modified perfluorotributylamine (PFTBA) nanoemulsions (HP NPs) were used for tumor treatments, named "contact-electrodynamic therapy (CEDT)" (Scheme 1). The generated ROS induces immunogenic cell death (ICD) in tumor cells, promotes the polarization of macrophages to M1 type, reverses
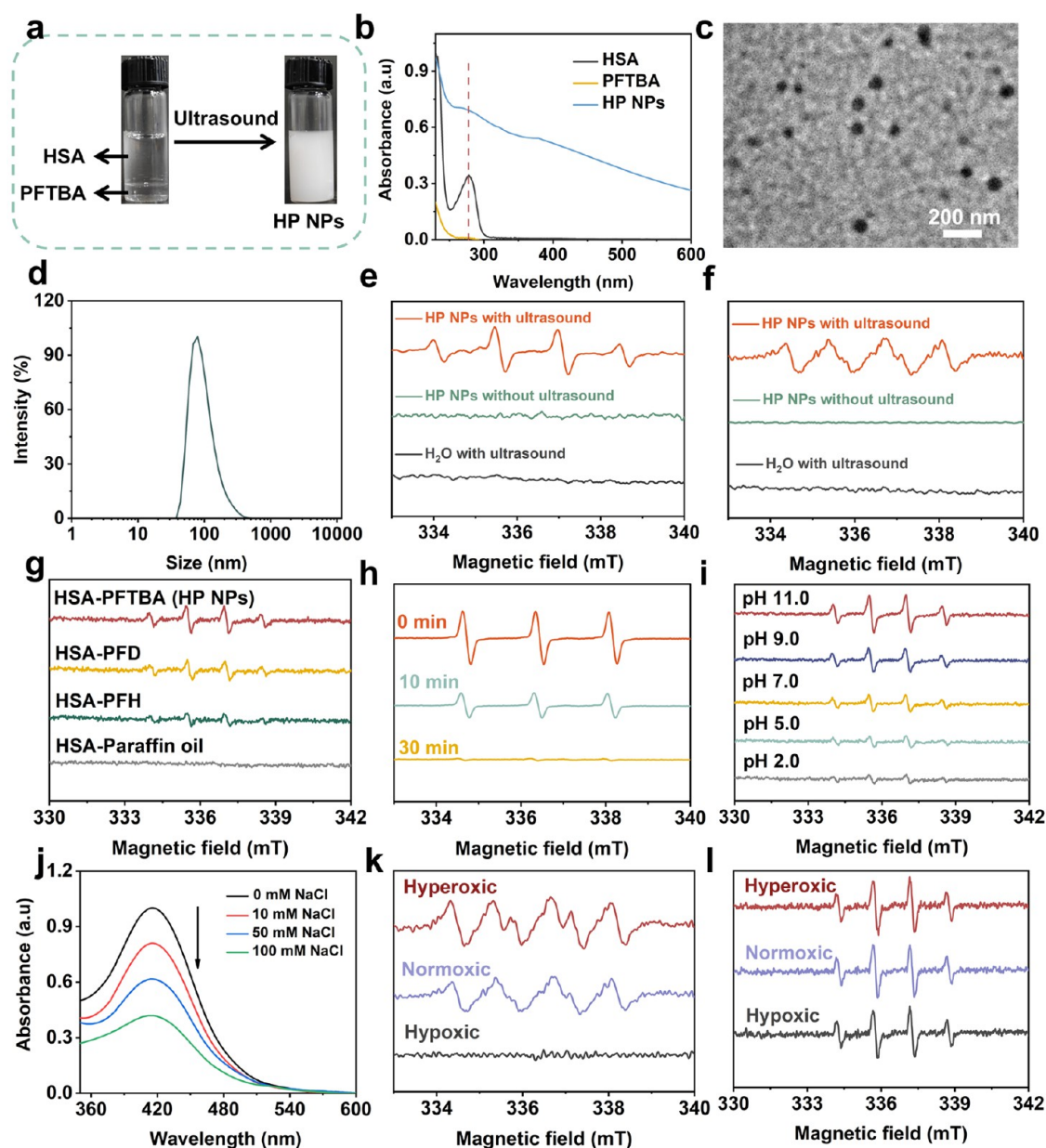
Figure 1. Characterization of HP NPs and ROS generation mechanism in ultrasonication-induced high-frequency liquid−liquid contact. (a) Preparation diagram and photograph of HP NPs. (b−d) Absorption spectra (b), TEM image (c), and hydrodynamic diameters (d) of HP NPs. (e) DMPO-•OH and (f) DMPO-•O$_2^-$ ESR spectra of HP NPs and H$_2$O treated with or without ultrasonication. (g) DMPO-•OH ESR spectra of solutions treated with different PFC nanoemulsions. (h) ESR spectra of TEMPO treated with HP NPs under different ultrasonication times. (i) DMPO-•OH ESR spectra of HP NPs treated at different pH values. (j) Absorption spectra of the OPD solution treated with HP NPs at different NaCl concentrations. (k) DMPO-•O$_2^-$ and (l) DMPO-•OH ESR spectra of HP NPs treated at different O$_2$ concentrations.

the tumor immunosuppressive microenvironment, accelerates the maturation of dendritic cells (DCs), actively presents tumor-associated antigens to T cells, activates the body's adaptive immune response, and finally achieves effective antitumor therapy. It is noteworthy that •OH is the main ROS generated in the liquid−liquid contact, which is not constrained by endogenous substances (i.e., O$_2$, H$_2$O$_2$, etc.) in the tumor microenvironment.

RESULTS AND DISCUSSION

As shown in Scheme 1, HSA-PFC nanoemulsions were prepared by a typical ultrasonic emulsification method.[24] HSA was utilized as the stabilizer to increase the water solubility and stability of HSA-PFC nanoemulsions (Figure 1a). As a clinically approved perfluorocarbon, PFTBA was mainly used for the subsequent studies. The UV−vis absorption spectra of HSA-PFTBA nanoemulsions (HP NPs) have the characteristic absorption peaks of HSA (Figure 1b), which proved the successful HSA modification of HP NPs. Transmission electron microscopy (TEM) images showed that the HP NPs had a uniform size (Figure 1c) with an average particle size of 62.5 ± 1.8 nm (Figure S1). The hydrodynamic size of the HP NPs determined by dynamic light scattering (DLS) was 77.4 ± 1.8 nm (Figure 1d). The ζ potential of HP NPs is −33 mV at pH 7.0, which can maintain the stability of HP NPs in the solution. The hydrodynamic size of the HP NPs in aqueous solution did not change significantly after
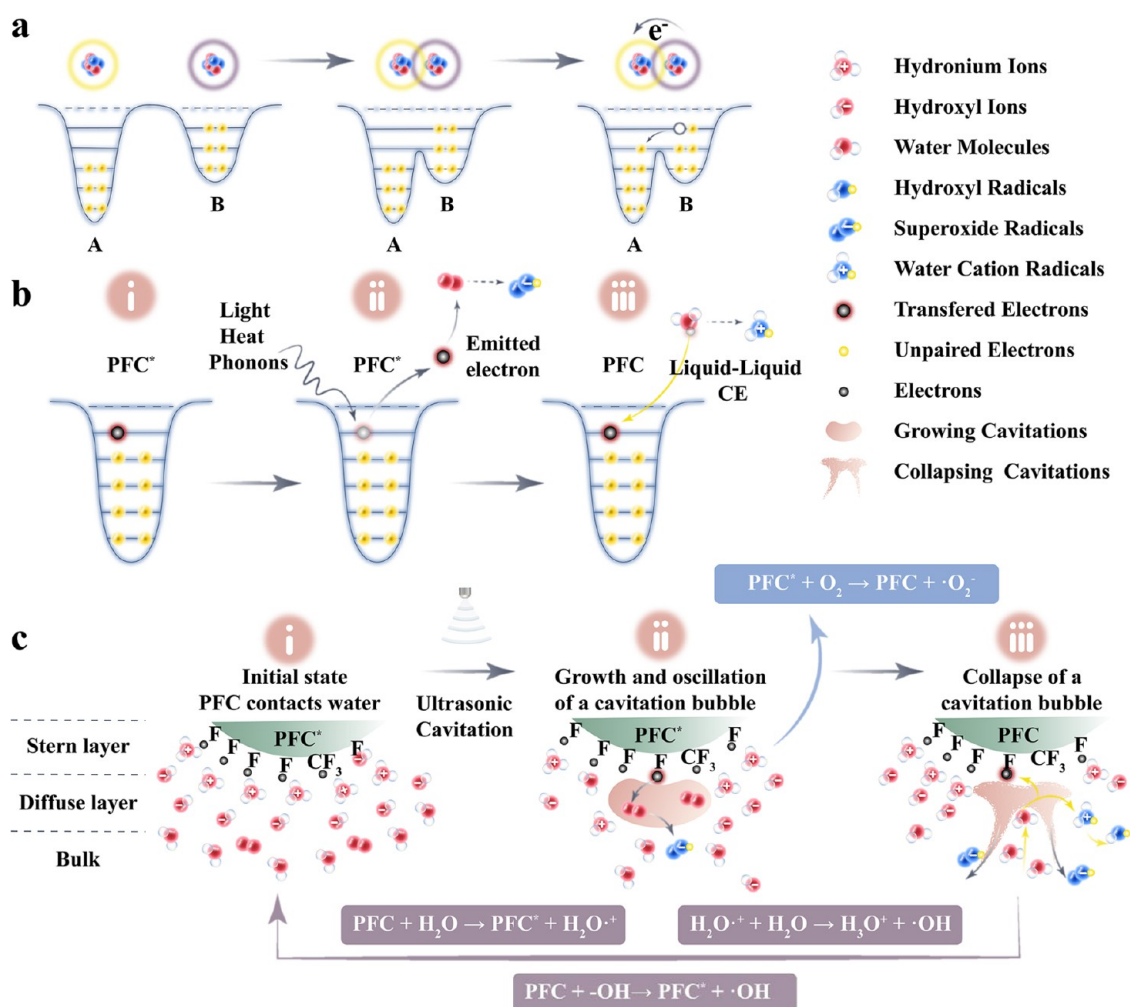
Figure 2. Schematic illustration of the ROS generation mechanism in liquid−liquid contact electrification. (a) Illustration of electron transfer induced by the electron cloud overlap between two atoms. (b) Description of electron transfer during contact electrification at the PFC−water "liquid−liquid" interface. (c) Schematic diagram of the redox reaction in ultrasonication-induced high-frequency liquid−liquid contact between PFC and water.

storage in aqueous solution for 72 h, demonstrating the excellent stability of HP NPs (Figure S2). Electron spin resonance (ESR) spectra were used to detect the ROS free radicals generated in the PFC−water "liquid−liquid" contact. The signals of 5,5-dimethyl-1-pyrroline N-oxide (DMPO)-$^\bullet$OH adducts were observed after HSA-PFTBA (HP NPs) and PFTBA were sonicated with DMPO for 30 min, respectively, while almost no signal was observed in the H$_2$O and HSA groups that were sonicated with DMPO (Figures 1e and S3). These results demonstrated the generation of $^\bullet$OH via electron transfer under ultrasonica-tion-induced high-frequency contact/separation in the PFTBA−water "liquid−liquid" interface.[19] Moreover, it has been reported that the high-frequency vibration of ultrasound also causes electron exchange at the solid−gas interface, allowing O$_2$ us to obtain electrons to produce $^\bullet$O$_2^-$. Therefore, the ESR spectra were also used to characterize the production of $^\bullet$O$_2^-$ during ultrasonication-induced high-frequency contact and separation in the PFTBA−water "liquid−liquid" interface. As shown in Figure 1f, the ultrasound group showed an obvious ESR signal of DMPO-$^\bullet$O$_2^-$, while the Control group without ultrasonication did not, demonstrating that $^\bullet$O$_2^-$ was generated during the ultrasonication process.[10] In addition, the

ESR signal of DMPO-$^\bullet$O$_2^-$ was not detected in the solution without HP NPs (H$_2$O group) under the same ultrasonication (Figure 1f).

Although it has been reported that ROS free radicals (i.e., $^\bullet$OH and $^\bullet$O$_2^-$) can be produced by water sonolysis under ultrasound, these free radicals were not detected in our work in the absence of PFC nanoemulsions (Figure 1e,f), indicating that the ROS free radicals are not produced by the reported water sonolysis mechanism.[25] In order to verify the ROS production mechanism, perfluorodecalin (PFD)\perfluorohex-anes (PFH)\paraffin oil with different F contents were prepared into nanoemulsion using the same method to investigate the level of $^\bullet$OH production (Figure 1g). The results show that the generated $^\bullet$OH signal intensities are consistent with F contents in the nanoemulsions, that is [$^\bullet$OH]$_{(PFTBA)}$ > [$^\bullet$OH]$_{(PFD)}$ > [$^\bullet$OH]$_{(PFH)}$ > [$^\bullet$OH]$_{(paraffin~oil)}$, and almost no signal is detected in the F-free paraffin oil nanoemulsion. This can be attributed to the stronger electronegativity of nanoemulsion with higher F contents, which can capture more electrons from water to produce $^\bullet$OH.[8] To further verify the electron transfer in liquid−liquid contact separation between water and PFC, the ESR spectra of 2,2,6,6-tetramethylpiperidine-1-oxyl (TEMPO) treated with
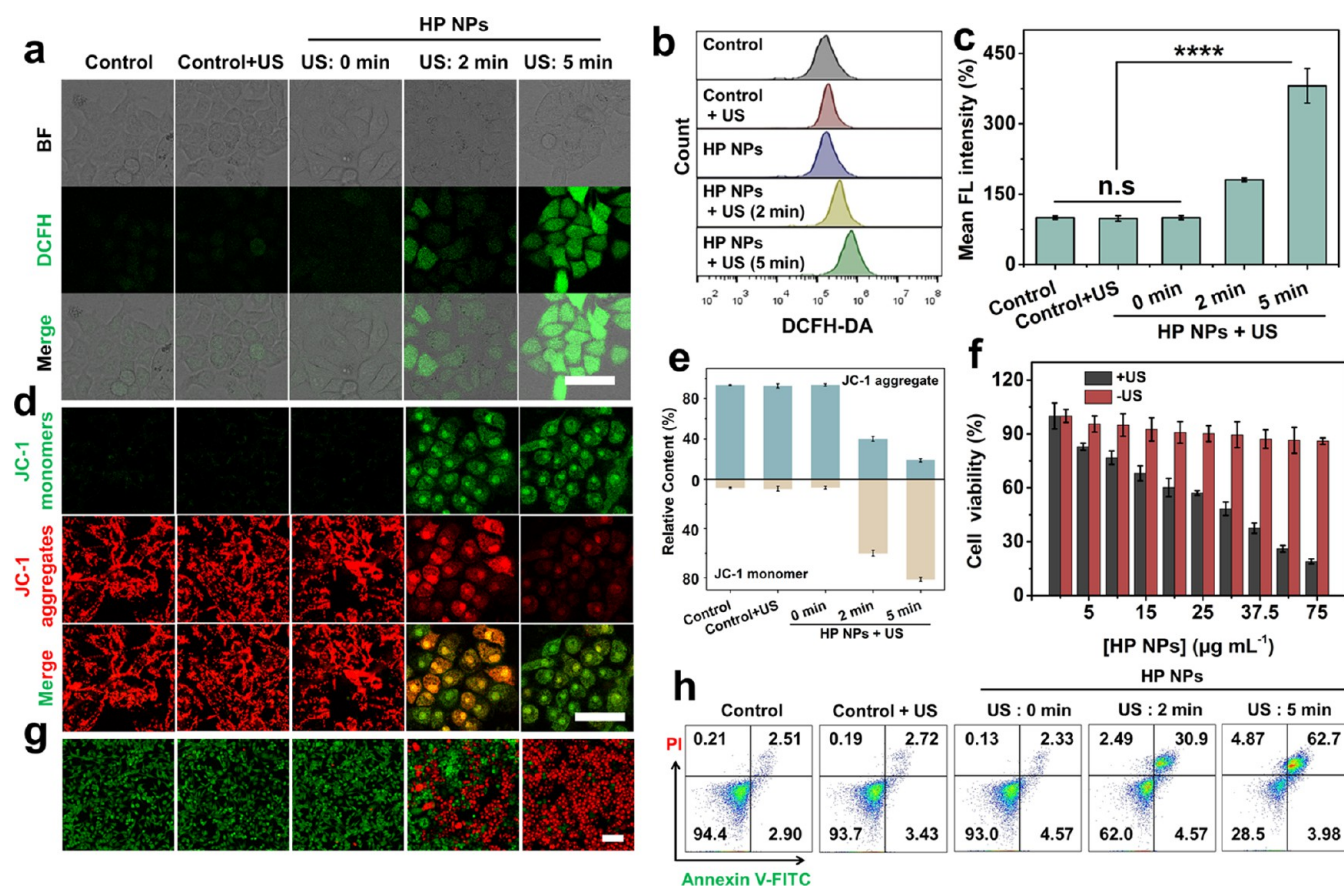
Figure 3. ROS generation performance of HP NPs in cells. (a) Representative confocal fluorescence imaging of 4T1 cells coincubated with HP NPs under different ultrasonication (US) times. Scale bar: 50 μm. (b) FCAS of ROS in 4T1 cells under different treatments, and (c) the corresponding fluorescence intensity. (d) Representative confocal fluorescence imaging and (e) FCAS of mitochondrial membrane potential changes in 4T1 cells under different treatments. JC-1 was a probe. Scale bar: 50 μm. (f) Cell viability analysis of 4T1 incubated with different concentrations of HP NPs with and without ultrasonication. (g) Confocal fluorescence imaging and (h) FCAS of 4T1 cells under different treatments. Scale bar: 100 μm. Error bars represent standard deviation based on three replicate data ($n = 3$). The statistical significance analysis was determined using Student's t test (two-group analysis) or one-way analysis of variance (ANOVA) (multigroup analysis). n.s. not significant, *$p <$ 0.1, **$p <$ 0.01, ***$p <$ 0.001, ****$p <$ 0.0001.

HP NPs under different ultrasonication times were measured (Figure 1h). If electron transfer occurs in liquid−liquid contact separation between water and PFC nanoemulsions, the stabilized radical TEMPO can react with 1 electron and 1 hydronium ion to form nonparamagnetic TEMPOH, which reduces the ESR signal of TEMPO. As shown in Figure 1h, after being treated with sonication in the presence of HP NPs, the TEMPO signal intensity decreases rapidly with the sonication time, while the ESR signal of TEMPO under the same ultrasonication without HP NPs is not significantly reduced (Figure S4), which proves that the electron transfer occurs in the ultrasonication-induced high-frequency liquid−liquid contact between water and PFC.[10]

In order to confirm whether the electron transfer of •OH production comes from H_2O or OH^-, the •OH production at different pH values was measured by ESR and O-phenylenedi-amine (OPD).[19] As shown in Figure 1i, the ESR signals belonging to DMPO-•OH are significantly enhanced as the solution pH increases from 2.0 to 11.0, indicating that part of the transferred electrons originate from the free OH^- of the solution. Notably, obvious ESR signals of DMPO-•OH still can be detected at pH 2.0, indicating that the transferred electrons are derived from not only free OH^-, but also H_2O, because the concentration of free OH^- is too low at pH 2.0 (10^{-12} mol

L^{-1}) to produce sufficient •OH. OPD was also used as a probe to investigate the effect of pH on •OH production, which can be oxidized by •OH to 2,3-diaminothiazine (DAP) with an absorption peak at 424 nm.[12] As shown in Figure S5, the absorbance value of DAP at 424 nm increased with an increase in pH, which is consistent with the ESR results. Furthermore, the effect of the ion concentration on the production of •OH was explored by the OPD (Figure 1j). The results showed that the characteristic absorption peak of DAP gradually decreased with the increase of NaCl concentration, indicating the decreased amount of •OH production. This may be attributed to the free ion shielding effect of NaCl, which hindered the electron-transfer process for producing •OH.[5,26]

Subsequently, the effects of oxygen levels in water on ROS production were explored. Oxygen levels were regulated by bubbling water with oxygen for the hyperoxic group or with nitrogen for the hypoxic group, and the normoxic group was not treated with the bubbling process. As shown in Figure 1k, compared to that of the normoxic group, the ESR signal of DMPO-•O_2^- significantly decreased and was almost undetect-able in the hypoxic group but significantly enhanced in the hyperoxic group, demonstrating that •O_2^- was generated from O_2 during electron exchange during ultrasonication. The possible mechanism is that the ultrasonication causes high-
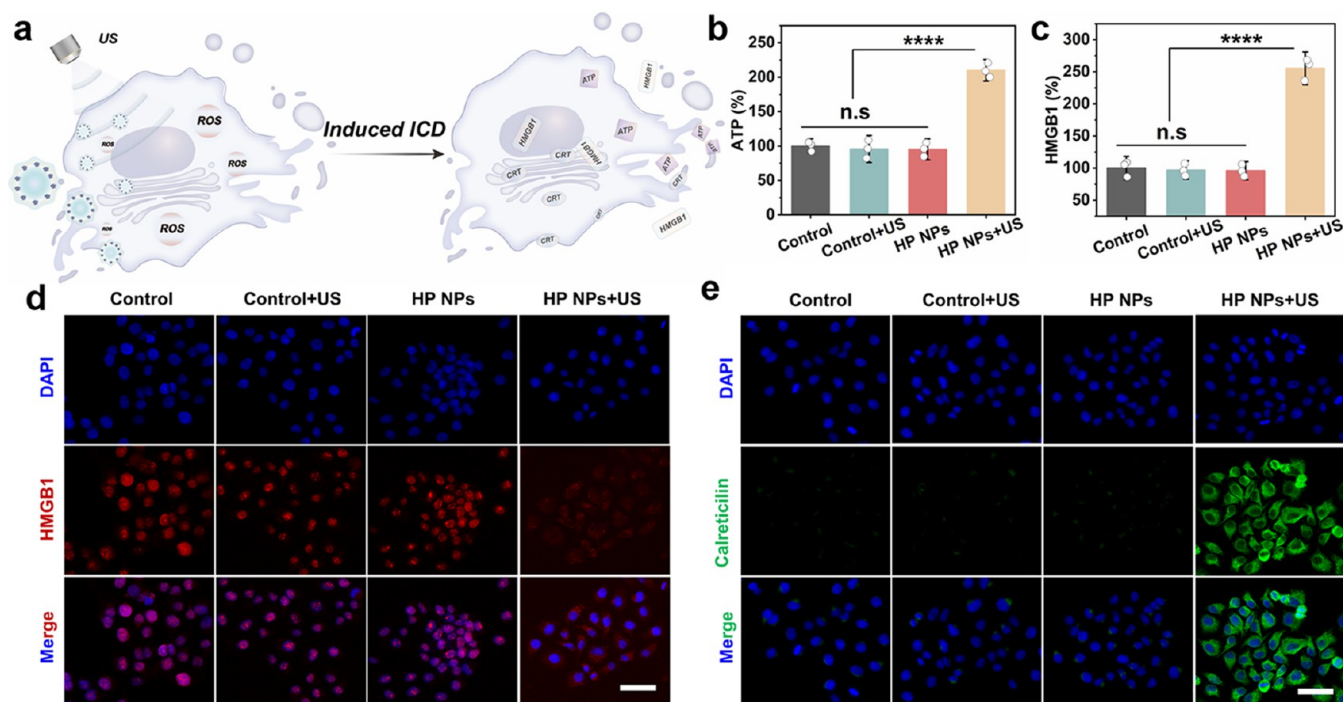
Figure 4. HP NP-induced ICD. (a) Schematic representation of HP NP-induced ICD. Relative percentages of (b) ATP and (c) HMGB1 content in the extracellular environment of 4T1 cells under different treatments. Representative fluorescence imaging of (d) HMGB1 and (e) calreticulin expressed by 4T1 cells under different treatments. Scale bar: 50 μm. Error bars represent standard deviation based on three replicate data ($n = 3$). The statistical significance analysis was determined using Student's t test (two-group analysis) or one-way analysis of variance (ANOVA) (multigroup analysis). n.s. not significant, *$p < 0.1$, **$p < 0.01$, ***$p < 0.001$, ****$p < 0.0001$.

frequency liquid−gas contact electrification between PFC and O_2, and the electron transforms from negatively charged PFC to O_2 to obtain $^\bullet O_2^-$. It is worth noting that the oxygen levels in water do not affect the level of $^\bullet OH$ production (Figure 1l), suggesting that the $^\bullet OH$ generated from liquid−liquid mixtures can be used to construct effective anticancer therapeutic modalities that are not restricted by the hypoxic tumor microenvironment.

Based on the above results, we speculated on the ROS generation mechanism in liquid−liquid contact electrification (Figure 2). First, the overlap of the electron cloud between the F atoms in PFC nanoemulsions and the O atoms in water lowers the energy barrier of the transition between the two states and enables electron transfer from water (H_2O and OH^-) to the PFC nanoemulsions during the liquid−liquid contact. At this moment, OH^- loses electrons to be oxidized to $^\bullet OH$ and H_2O loses electrons to be oxidized to the hydronium ion (H_3O^+), which is ultimately converted to $^\bullet OH$ (Figure 2a).[7] At the same time, the PFC is negatively charged (labeled as PFC*) due to the interfacial electron exchange (Figure 2b, State (i)). The ions can accumulate on the surface of the negatively charged PFC* to form an electrostatic double-layer structure (diffuse layer + stern layer) at this time (Figure 2c, State (i)).[11] When the ultrasonication is applied, O_2 dissolved in water forms cavitation bubbles (Figure 2c, State (ii)), which can gain electrons by liquid−gas contact electrification to form $^\bullet O_2^-$, and the PFC* loses electrons into uncharged PFC (Figure 2b, States (ii) and (iii)).[11] When the cavitation bubbles exploded violently, the microjet caused water to be projected onto the surface of the PFC (Figure 2c, State (iii)), initiating the next cycle of liquid−liquid contact: PFC gains electrons to carry a negative charge and water loses electrons

to produce $^\bullet OH$.[27] The experimental results confirmed that HP NPs can generate ROS via electron transfer at the liquid− liquid interface under ultrasonication, which is different from the mechanism of conventional SDT that generates ROS through the cavitation effect.[28,29] This mechanism may provide some new understanding of SDT in which liquid−liquid contact electrification induced ROS generation may coexist in SDT. Importantly, the raw material for producing $^\bullet OH$ by electron transfer from interfacial contact is water (including H_2O and OH^-), which is abundant in the body, so the ROS generation is not limited by endogenous substances in the tumor microenvironment.

The tumor-killing effect of the ROS generated by HP NPs was verified at the cellular level. First, the probe 2′,7′-dichlorodihydrofluorescein diacetate (DCFH-DA) was used to determine intracellular ROS levels,[30] and changes in ROS levels induced by HP NPs were visualized by a confocal laser scanning microscope (CLSM), and the results are shown in Figure 3a. Similar to the Control group, HP NPs did not produce obvious green fluorescence in the cells without ultrasonication (as shown in the "HP NPs+US 0 min" group). In contrast, the intracellular ROS level in the ultrasonication-treated group significantly increased, which resulted in a more obvious green fluorescence. With prolonged ultrasonication time, more ROS were produced in the cells, and the 5 min ultrasonication-treated group showed a stronger green fluorescence intensity that was 3.8 times higher than that of the "HP NPs+US 0 min" group. The ultrasonication-enhanced ROS accumulation was further validated by the results of flow cytometry (FCAS) (Figure 3b,c). It has been extensively documented that ROS can induce mitochondrial damage, which is one of the causes of large-scale apoptosis of tumor cells, so the classical JC-1 probe was used to stain the
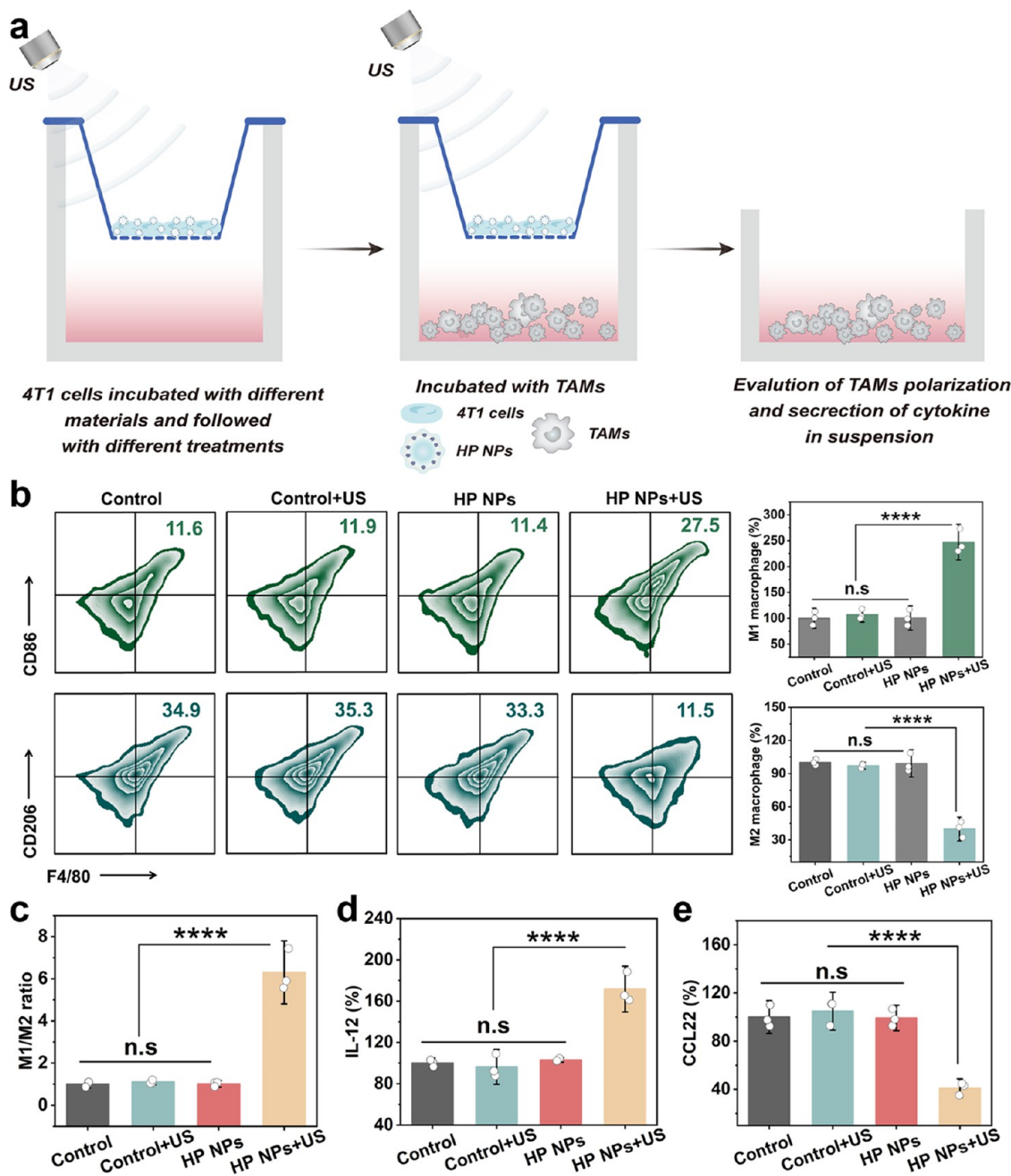
Figure 5. HP NP-mediated macrophage polarization *in vitro*. (a) Design of the transwell system for studying macrophage polarization. (b) Representative FCAS of macrophage differentiation into M1 macrophages (F4/CD80$^+$CD86$^+$) and M2 macrophages (F4/CD80$^+$CD206$^+$), and (c) the corresponding M1/M2 ratio. Relative percentages of (d) IL-12 and (e) CCL22 in macrophage polarization. Error bars represent standard deviation based on three replicate data (n = 3). The statistical significance analysis was determined using Student's *t* test (two-group analysis) or one-way analysis of variance (ANOVA) (multigroup analysis). n.s. not significant, *$p < 0.1$, **$p < 0.01$, ***$p < 0.001$, ****$p < 0.0001$.

mitochondria of 4T1 cells.[19,31] As shown in confocal imaging of 4T1 cells (Figure 3d), HP NP-cultured cells exhibited stronger green fluorescence of the JC-1 monomer than that of the Control group under ultrasonication, indicating the mitochondrial depolarization of 4T1 cells. The mitochondrial depolarization quantified by FCAS (Figure 3e) shows results similar to those of confocal imaging experiments. Subsequently, MTT assays were used to evaluate the killing effect of HP NPs on 4T1 tumor cells. As shown in Figures 3f and S6, HP NPs without ultrasonication had extremely low cytotoxicity and maintained cell viability above 85% even at a concentration of 75 μg mL^{-1}. However, when ultrasonication

was applied, the survival of 4T1 cells incubated with HP NPs was drastically reduced to only 19% at a concentration of 75 μg mL^{-1}, which was attributed to the ROS generated in ultrasonication-induced high-frequency liquid−liquid contact. Furthermore, ROS-mediated tumor killing was further validated by FCAS and live/dead cell staining.[30,32] As shown in Figure 3g, confocal fluorescence imaging of live/dead cell staining by calcein-AM/Propidium Iodide (PI) indicated that HP NPs induced tumor cell death in combination with ultrasonication, showing bright PI red fluorescence (labeling the dead cells), whereas the green fluorescence of FITC was almost absent (labeling the live cells). All of the results proved
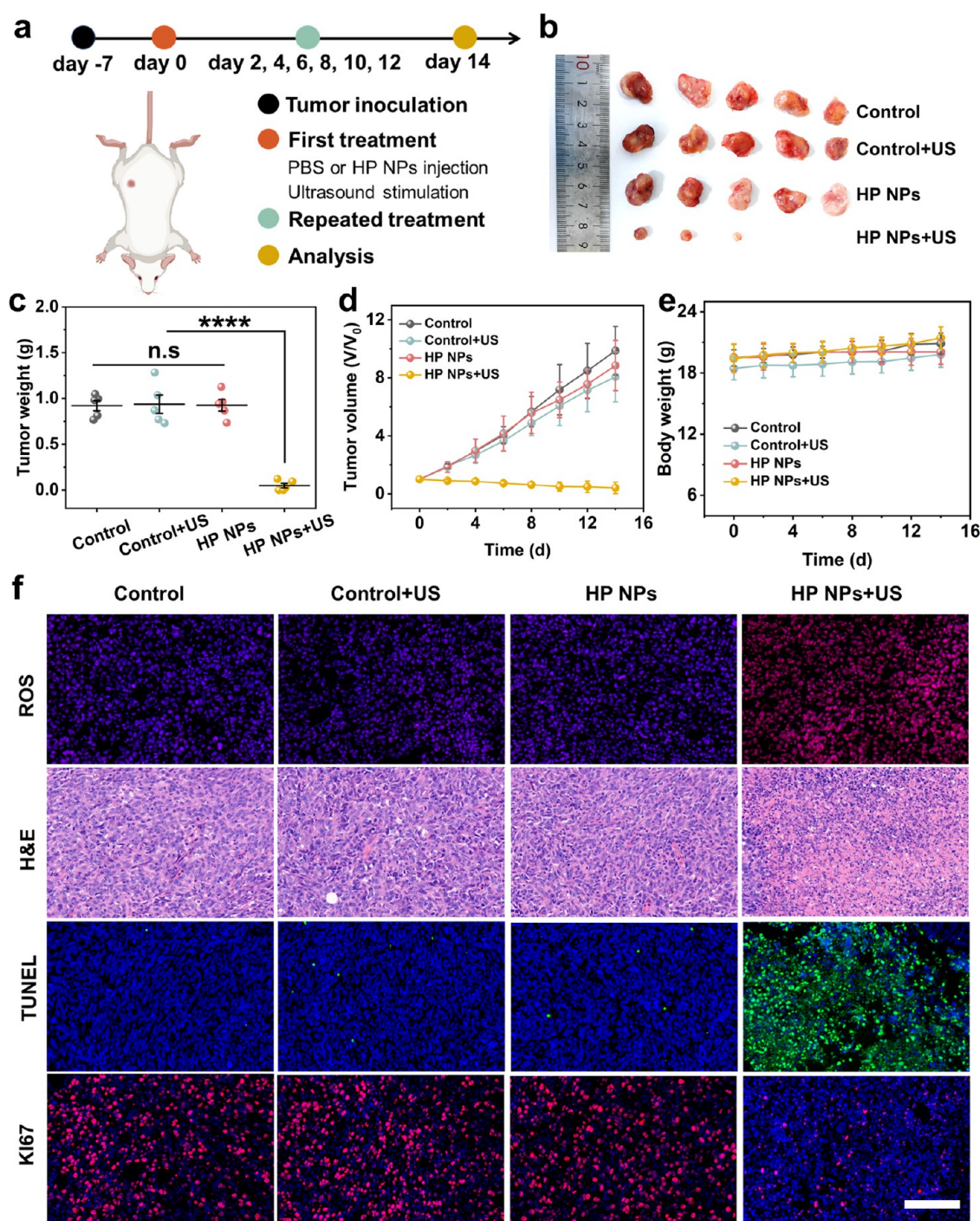
Figure 6. Evaluation of HP NP-mediated therapy in solid tumors. (a) Schematic illustration of 4T1 tumor-bearing mice model construction and treatment. (b) Photographs of tumors, (c) tumor weight, (d) tumor growth curves, and (e) body weight of mice under different treatments. (f) Representative microscopic images of ROS, H&E, TUNEL, and Ki67 staining of tumor areas. Scale bar: 100 μm. Error bars represent standard deviation based on five replicate data ($n = 5$). The statistical significance analysis was determined using Student's t test (two-group analysis) or one-way analysis of variance (ANOVA) (multigroup analysis). n.s. not significant, *$p < 0.1$, **$p < 0.01$, ***$p < 0.001$, ****$p < 0.0001$.

that the HP NP-mediated generation of ROS had significant antitumor activity, killing almost all tumor cells. Additionally, FCAS can reflect different periods of apoptosis by staining cells using PI and FITC (Figure 3h).[31] The results showed that the generated ROS resulted in an increase in the apoptosis rate of cells from 5.6% (Control group) to 71.5% (HP NPs+US 5 min), demonstrating that the HP NP-mediated generation of ROS has outstanding potential in tumor treatment.

Studies have indicated that ROS are capable of inducing ICD in cells, resulting in the release of a range of damage-associated molecular patterns (DAMPs), such as calreticulin eversion, high-mobility group box 1 (HMGB1) migration, and ATP secretion into the extracellular environment (Figure 4a).[30,33,34] As shown in Figure 4b, the ATP levels secreted into the extracellular environment were measured by an ATP detection kit. The results showed that the ATP secretion levels of the Control, Control+US, and HP NPs groups had no
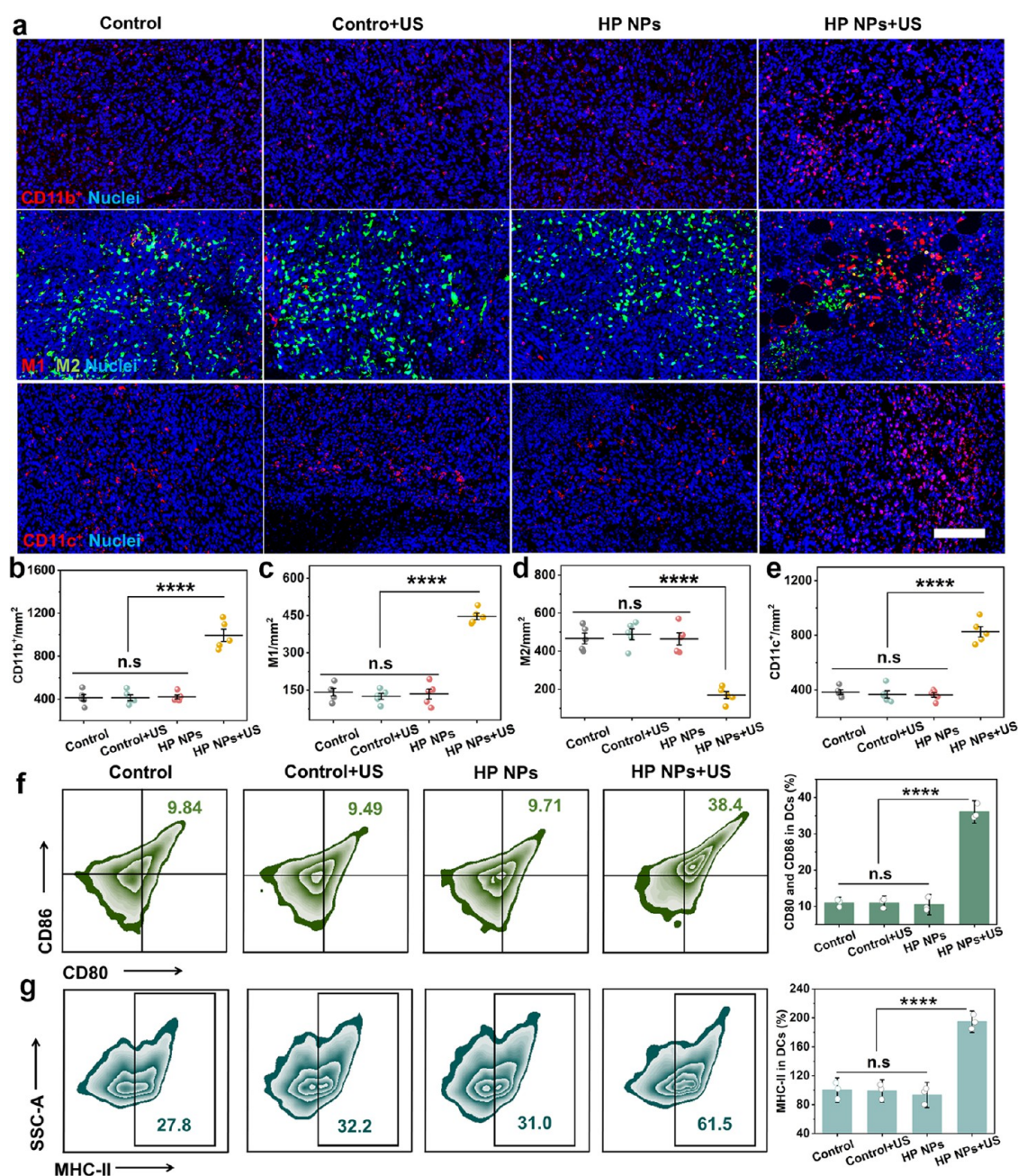
Figure 7. Recruitment and maturation of antigen-presenting cells in the HP NP-mediated therapy. (a) Representative immunofluorescence images of the distribution of CD11b^{+}, M1/M2, and CD11c^{+} in the tumor tissues after 14 days of different treatments. Scale bar: 100 μm. The corresponding quantitative histogram of immunofluorescence staining of (b) CD11b^{+}, (c) M1, (d) M2, and (e) CD11c^{+} in the tumor tissues. FCAS of (f) CD80/CD86 and (g) MHC-II in TDLNs of different groups after 14 days of different treatments and the corresponding histograms of quantitative analysis. Error bars represent standard deviation based on three or five replicate data. The statistical significance analysis was determined using Student's t test (two-group analysis) or one-way analysis of variance (ANOVA) (multigroup analysis). n.s. not significant, *$p <$ 0.1, **$p <$ 0.01, ***$p <$ 0.001, ****$p <$ 0.0001.

significant differences. However, HP NPs could cause a significant increase in the ATP content released into the external environment of 4T1 cells after applied ultrasonication (the HP NPs+US group), expressing the "find me" signal to attract antigen-presenting cells (APCs) to phagocytose dead cancer cells.[30] Additionally, enzyme-linked immunosorbent assay (ELISA) results demonstrated that the HP NPs+US group also induced higher levels of HMGB1 exposure than did the Control group (Figure 4c). Similar phenomena were observed in the confocal fluorescence imaging results of HMGB1 migrating from the nucleus to the extracellular space

(Figure 4d), as well as the transfer of calreticulin from the endoplasmic reticulum to the cell surface (Figure 4e). The results showed that the HP NPs+US group expressed the highest calreticulin (green fluorescence) and HMGB1 (red fluorescence), which could release "danger" signals to promote the exercise of antigen presentation by APCs and activate the body's immune response.[33,35]

Tumor-associated macrophages (TAMs) are the most important antigen-presenting and immunosuppressive cells in tumors and are closely associated with tumor development.[36,37] Thus, macrophage (RAW 264.7) polarization-
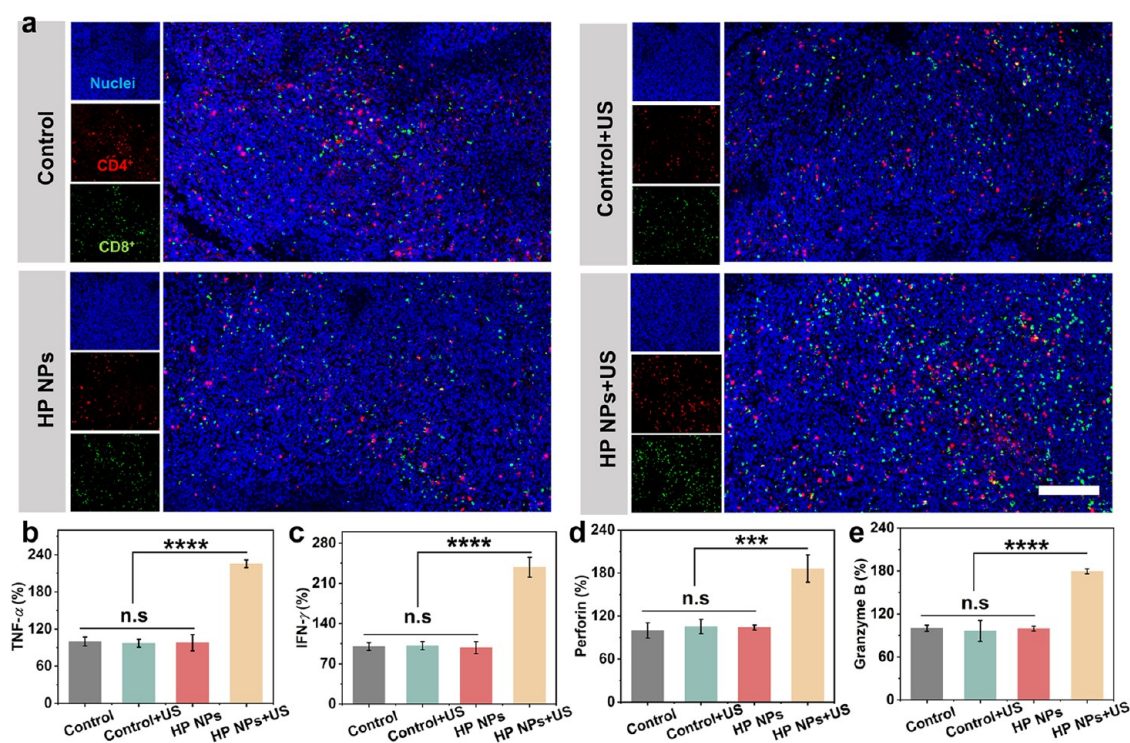
Figure 8. Immune activation of T cells in the HP NP-mediated therapy. (a) Representative immunofluorescence images of the distribution of CD4+/CD8+ T cells in the tumor tissues of different groups. Scale bar: 200 μm. Percentage of cytokine (b) TNF-α, (c) IFN-γ, (d) perforin, and (e) granzyme B content from tumors of each group. Error bars represent standard deviation based on three replicate data. The statistical significance analysis was determined using Student's t test (two-group analysis) or one-way analysis of variance (ANOVA) (multigroup analysis). n.s. not significant, *$p < 0.1$, **$p < 0.01$, ***$p < 0.001$, ****$p < 0.0001$.

mediated innate immune responses were explored *in vitro*. Macrophages were incubated with 4T1 cells for 48 h after different pretreatments in the transwell system. Then, the phenotype of the macrophages was analyzed by measuring the corresponding characteristic cytokine expression (Figure 5a). FCAS results showed a lower positive rate of M2 phenotype (F4/CD80+CD206+, immunosuppressive) and a higher positive rate of M1 phenotype (F4/CD80+CD86+, immunostimulatory) in the HP NPs+US group than that in the Control, Control+US, and HP NPs groups (Figure 5b,c), suggesting that HP NPs has an effective polarizing effect on macrophages under ultrasonication.[36,38] Meanwhile, ELISA kits were used to detect cytokines interleukin (IL)-12 associated with M1 macrophage differentiation and CCL22 associated with M2 macrophage differentiation (Figure 5d,e).[30] The results showed that the HP NPs+US caused a 1.7-fold increase in IL-12 secretion and a 59% decrease in CCL22 secretion relative to the Control group. All these results suggested that ROS produced in the liquid–liquid contact can trigger ICD, which has the potential to activate the body's innate immune response (M1-polarization of the RAW 264.7 macrophages).[39]

The antitumor efficacy of HP NP-mediated therapy was evaluated in tumor-bearing mice. As shown in Figure 6a, the tumor-bearing mice model was constructed by injecting 4T1 cells directly subcutaneously. After 14 days of treatment, the mice were sacrificed, and the relevant data are recorded as shown in Figure 6b–e. As expected, the tumors of mice in the Control group without the administration of HP NPs maintained a rapid growth rate even with the assistance of ultrasonication (Figure 6b–d).[40] After the administration of HP NPs (the HP NPs group), the tumor continued to maintain a growth rate similar to that of the Control group. However, after the ultrasonication was applied (the HP NPs +US group), tumor growth was significantly inhibited, and solid tumors were even completely eliminated. Meanwhile, the mice remained healthy during the treatment, and there was no significant difference in the weight of mice in each group during the complete 14-day observation period (Figure 6e). Subsequently, the ROS generated in the tumor tissues were verified by dihydroethidium. As shown in Figure 6f, tumor cells in the HP NPs+US group produce higher levels of ROS. A strong red fluorescence from the intracellular ROS probe can be observed in the tumor tissue, proving that HP NPs exert therapeutic effects in the intracellular and cause damage to tumor tissue.[18] The results of hematoxylin and eosin (H&E) and transferase-mediated deoxyuridine triphosphate nick end labeling (TUNEL) staining verified the ROS-mediated tumor killing, and the HP NPs+US group showed more severe apoptosis than other three groups.[41] Ki67 staining further demonstrated that the HP NPs+US group severely affected the proliferation of tumor cells.[42,43] All of these results confirm that the ROS generated in liquid–liquid contact exhibit excellent tumor suppressive ability.

The antitumor mechanism mediated by HP NPs is further demonstrated by activated immune responses *in vivo*. Briefly, ROS induces ICD of tumor cell to release tumor-associated antigens, which can attract the recruitment of APCs, and present antigenic peptides to T cells to trigger an adaptive immune response to reverse tumor immunosuppressive microenvironment.[41] As shown in Figure 7a,b, macrophages (CD11b+) of treated tumor-bearing mice aggregate at the tumor site and regulate the transition of tumor-associated

macrophages (TAMs) from M2-like phenotype to M1-like phenotype (Figure 7c,d).[34,43] The number of M1-TAMs in the HP NPs+US group was approximately 3.1-fold higher than that of the Control group, while the number of M2-TAMs decreased by 53.6% compared to the Control group, demonstrating that the reversal of macrophage phenotype successfully converted the tumor microenvironment from "cold" to "hot".[33,44] In addition, as one of the important antigen-presenting cells, DCs (CD11c$^+$) also massively infiltrate the tumor sites of tumor-bearing mice after treatment (Figure 7e), integrate antigen signals from tumor cells, and migrate to mature in tumor-draining lymph nodes (TDLNs) to present antigen to T cells.[45,46] Thus, TDLNs in the treated groups were determined by FCAS to study the maturation of DCs (Figure 7f,g).[35] As expected, there was no significant difference in the number of mature DCs (CD80$^+$CD86$^+$) in the three groups, Control, Control+US, and HP NPs. In sharp contrast, the percentage of mature DCs in the HP NPs+US group increased by 3.2 times compared with the Control group and expressed a large number of antigen-presenting molecules MHC-II to present antigens to the T cell, which contributed to T cell activation.[47] Immunofluorescence staining of tumor tissues revealed that the recruitment of T cells in tumor tissues was significantly increased compared with the Control group and further differentiated into cytotoxic CD4$^+$/CD8$^+$ T cells (Figure 8a).[48] At the same time, activated T cells also kill cancer cells by secreting tumor necrosis factor (TNF)-α, interferon (IFN)-γ, granzyme B, and perforin (Figure 8b–e), activate apoptosis signaling pathway, and induce the body's powerful antitumor immune response.[30]

The potential biosafety of the HP NP-mediated therapy was evaluated. Blood and serum were collected from each group of mice for hematological analysis and biochemical indicator tests.[22,34] The results showed that the values of white blood cells in the treated mice were lower than those in the Control group, and there were no obvious abnormalities in the liver and kidney function indexes of the mice (Figure S7). Moreover, no obvious lesions were observed in the H&E staining results of the main organs (heart, liver, spleen, lung, and kidney) of the tumor-bearing mice in each group after the treatment period (Figure S8),[34,43] which proved the excellent biosafety of HP NP-mediated contact-electro-dynamic therapy (CEDT).

CONCLUSIONS

In summary, we have proposed a perfluorocarbon–water "liquid–liquid" interface system and demonstrated that electron transfer occurred during liquid–liquid contact electrification and the induced interfacial redox reactions can generate ROS. HSA-modified perfluorocarbon nanoemulsions were prepared to construct the perfluorocarbon–water "liquid–liquid" interface, which generated a high-frequency liquid–liquid contact by ultrasonication. During the high-frequency liquid–liquid contact, electrons can be transferred from H$_2$O and OH$^-$ to perfluorocarbon to produce $^\bullet$OH, and O$_2$ in water can gain electrons from negatively charged perfluorocarbon (PFC*) to produce $^\bullet$O$_2^-$. Based on this ROS generation mechanism, the HSA-PFTBA nanoemulsions (HP NPs) were used for the treatment of tumors by ROS-mediated apoptosis of tumor cells, named "contact-electro-dynamic therapy (CEDT)". This therapy has the following advantages: (1) the production of $^\bullet$OH is not constrained by endogenous components (i.e., O$_2$, H$_2$O$_2$, etc.) in the tumor microenviron-

ment; (2) the ultrasonication-mediated CEDT is a noninvasive and deep-penetrating technology with minimal damage to normal tissues; (3) PFTBA is a clinically approved perfluorocarbon, which endows HP NPs with good biosafety and emerging prospect for clinical applications; and (4) it can awaken the body's immune response to enhance the antitumor effect. This work provides new insights into the generation of free radicals during contact electrification at the liquid–liquid interface and also provides a new tumor therapeutic modality that is not limited by endogenous substances in the tumor microenvironment.

EXPERIMENTAL SECTION

Materials. O-Phenylenediamine (OPD) was purchased from Sinopharm Chemical Reagent Co., Ltd. (Shanghai, China). Perfluorotributylamine (PFTBA), perfluorodecalin (PFD), perfluorohexanes (PFH), and paraffin oil were obtained from Makclin Biochemical Co., Ltd. (Shanghai, China). Other chemicals were obtained from Makclin Biochemical Co., Ltd. (Shanghai, China) or Sigma-Aldrich (St. Louis, MI). Milli-Q water with a resistivity of 18.2 MΩ cm^{-1} was used in all of the experiments. All chemicals and reagents were used as received without any further purification.

Characterization. TEM images and high-resolution TEM (HRTEM) of nanoparticles were captured using a JEM-F200 transmission electron microscope. ζ Potential measurements and hydrodynamic diameter were collected on a Malvern Zetasizer Nano ZS90 instrument with a temperature controller (25 °C). UV–vis spectra were collected on a Cary series ultraviolet–visible absorption spectrometer (Agilent Technologies). ESR spectra were obtained by an electron paramagnetic resonance (EPR) spectrometer (Bruker Magnettech ESR5000, Germany). Ultrasonication is generated by an acoustic dynamometer (NSE-UPH-I, China), and if not specified, the parameters of ultrasonication are 30 kHz and 2.0 W cm^{-2}.

Preparation of HP NPs. First, HSA (16 mg) was dissolved in H$_2$O (8 mL) and stirred for 4 h to form an HSA solution (2 mg mL^{-1}). Then, the HSA solution (2 mg mL^{-1}, 8 mL) was mixed with PFTBA (300 μL) and stirred for 20 min, and the mixed solution was sonicated for 20 min at 25 °C with a cell crusher (SCIENTZ-II D, China) to form HP NPs. Then, the solution of HP NPs was collected by ultrafiltration centrifugation. HSA-PFD, HSA-PFH, and HSA-paraffin oil were prepared by the same process as the above method.

Cell Culture Section. NALM6 cells, HeLa cells, 293 cells, COS7 cells, and 4T1 cells were purchased from Gaining Biological Co., Ltd. (Shanghai, China) and cultured in the DMEM medium or RMPI-1640 medium supplemented with 10% FBS and 1% streptomycin/penicillin at 37 °C standard cell incubator (5% CO$_2$).

Construction of a Tumor-Bearing Mice Model. The female BALB/c mice (5 weeks old) were purchased from the Wuhan Experimental Animal Center (Hubei, China). The tumor-bearing mice model was constructed by injecting 4T1 cells directly subcutaneously. The 4T1 tumor-bearing mice with tumor volume close to 100 mm^3 were randomly divided into four groups ($n = 5$ per group). The Control and Control+US groups were injected with PBS (dose: 100 μL) every 2 days, and the HP NPs and HP NPs+US groups were injected with HP NPs (dose: 4 mg kg^{-1}) every 2 days. Subsequently, ultrasonication (30 kHZ, 2.0 W cm^{-2}) was applied to the tumor sites of the mice in the Control+US and HP NPs+US groups. The tumor size and body weight of the mice were observed every 2 days, and the mice were sacrificed after 14 days. Then, the relevant data were recorded.

ASSOCIATED CONTENT

⬛ Supporting Information

The Supporting Information is available free of charge at https://pubs.acs.org/doi/10.1021/jacs.4c02149.

Detailed experimental methods, TEM images, hydrodynamic diameters, ESR spectra, absorption spectra, cell

viability analysis, hematological analysis and serum biochemical analysis, and H[TC8]&E staining images (PDF)

AUTHOR INFORMATION

Corresponding Authors

Yi Liu − State Key Laboratory of Separation Membrane and Membrane Process & Tianjin Key Laboratory of Green Chemical Technology and Process Engineering, School of Chemistry and Chemical Engineering, Tiangong University, Tianjin 300387, China; School of Chemical and Environmental Engineering, Wuhan Polytechnic University, Wuhan 430023, China; orcid.org/0000-0001-7626-0026; Email: yiliuchem@whu.edu.cn

Zhong Lin Wang − Beijing Institute of Nanoenergy and Nanosystems, Chinese Academy of Sciences, Beijing 100083, China; orcid.org/0000-0002-5530-0380; Email: zhong.wang@mse.gatech.edu

Peng Jiang − Department of Orthopedics Trauma and Microsurgery, Zhongnan Hospital of Wuhan University, School of Pharmaceutical Sciences, Wuhan University, Wuhan 430071, China; Key Laboratory of Combinatorial Biosynthesis and Drug Discovery (Ministry of Education), Wuhan University, Wuhan 430072, China; orcid.org/0000-0002-7380-593X; Email: jiangpeng@whu.edu.cn

Authors

Haimei Li − Department of Orthopedics Trauma and Microsurgery, Zhongnan Hospital of Wuhan University, School of Pharmaceutical Sciences, Wuhan University, Wuhan 430071, China; Key Laboratory of Combinatorial Biosynthesis and Drug Discovery (Ministry of Education), Wuhan University, Wuhan 430072, China

Zichen Wang − Department of Orthopedics Trauma and Microsurgery, Zhongnan Hospital of Wuhan University, School of Pharmaceutical Sciences, Wuhan University, Wuhan 430071, China

Xu Chu − State Key Laboratory of Separation Membrane and Membrane Process & Tianjin Key Laboratory of Green Chemical Technology and Process Engineering, School of Chemistry and Chemical Engineering, Tiangong University, Tianjin 300387, China

Yi Zhao − Department of Orthopedics Trauma and Microsurgery, Zhongnan Hospital of Wuhan University, School of Pharmaceutical Sciences, Wuhan University, Wuhan 430071, China

Guangqin He − Department of Orthopedics Trauma and Microsurgery, Zhongnan Hospital of Wuhan University, School of Pharmaceutical Sciences, Wuhan University, Wuhan 430071, China

Yulin Hu − Department of Orthopedics Trauma and Microsurgery, Zhongnan Hospital of Wuhan University, School of Pharmaceutical Sciences, Wuhan University, Wuhan 430071, China

Complete contact information is available at:
https://pubs.acs.org/10.1021/jacs.4c02149

Notes

The authors declare no competing financial interest.

ACKNOWLEDGMENTS

REFERENCES

(1) Fan, F. R.; Tian, Z. Q.; Wang, Z. L. Flexible triboelectric generator. Nano Energy 2012, 1, 328−334.

(2) Niu, S.; Wang, S.; Lin, L.; Liu, Y.; Zhou, Y. S.; Hu, Y.; Wang, Z. L. Theoretical study of contact-mode triboelectric nanogenerators as an effective power source. Energy Environ. Sci. 2013, 6, 3576−3583.

(3) Chen, Y.; Pu, X.; Liu, M.; Kuang, S.; Zhang, P.; Hua, Q.; Cong, Z.; Guo, W.; Hu, W.; Wang, Z. L. Shape-adaptive, self-healable triboelectric nanogenerator with enhanced performances by soft solid-solid contact-electrification. ACS Nano 2019, 13, 8936−8945.

(4) Lin, S.; Chen, X.; Wang, Z. L. Contact-electrification at the liquid-solid interface. Chem. Rev. 2022, 122, 5209−5232.

(5) Nie, J.; Ren, Z.; Xu, L.; Lin, S.; Zhan, F.; Chen, X.; Wang, Z. L. Probing contact-electrification-induced electron and ion transfers at a liquid-solid interface. Adv. Mater. 2020, 32, No. e1905696.

(6) Lin, S.; Zhu, L.; Tang, Z.; Wang, Z. L. Spin-selected electron transfer in liquid-solid contact-electrification. Nat. Commun. 2022, 13, No. 5230.

(7) Wang, Z. L.; Wang, A. C. On the origin of contact-electrification. Mater. Today 2019, 30, 34−51.

(8) Zhang, J.; Lin, S.; Wang, Z. L. Triboelectric nanogenerator array as a probe for in situ dynamic mapping of interface charge transfer at a liquid-solid contacting. ACS Nano 2023, 17, 1646−1652.

(9) Xu, C.; Zi, Y.; Wang, A. C.; Zou, H.; Dai, Y.; He, X.; Wang, P.; Wang, Y. C.; Feng, P.; Li, D.; Wang, Z. L. On the electron-transfer mechanism in the contact-electrification effect. Adv. Mater. 2018, 30, No. 1706790.

(10) Berbille, A.; Li, X. F.; Su, Y.; Li, S.; Zhao, X.; Zhu, L.; Wang, Z. L. Mechanism for generating H_2O_2 at water-solid interface by contact-electrification. Adv. Mater. 2023, 35, No. e2304387.

(11) Wang, Z.; Berbille, A.; Feng, Y.; Li, S.; Zhu, L.; Tang, W.; Wang, Z. L. Contact-electro-catalysis for the degradation of organic pollutants using pristine dielectric powders. Nat. Commun. 2022, 13, No. 130.

(12) Zhao, Y.; Liu, Y.; Wang, Y.; Li, S.; Liu, Y.; Wang, Z. L.; Jiang, P. The process of free radical generation in contact-electrification at solid-liquid interface. Nano Energy 2023, 112, No. 108464.

(13) Kari, J.; Molina, G. A.; Schaller, K. S.; Schiano-di-Cola, C.; Christensen, S. J.; Badino, S. F.; Sørensen, T. H.; Røjel, N. S.; Keller, M. B.; Sørensen, N. R.; Kolaczkowski, B.; Olsen, J. P.; Krogh, K. B. R. M.; Jensen, K.; Cavaleiro, A. M.; Peters, G. H. J.; Spodsberg, N.; Borch, K.; Westh, P. Physical constraints and functional plasticity of cellulases. Nat. Commun. 2021, 12, No. 3847.

(14) Pera-Titus, M.; Leclercq, L.; Clacens, J. M.; De Campo, F.; Nardello-Rataj, V. Pickering interfacial catalysis for biphasic systems: from emulsion design to green reactions. Angew. Chem., Int. Ed. 2015, 54, 2006−2021.

(15) Zhang, M.; Song, W.-Z.; Chen, T.; Sun, D.-J.; Zhang, D.-S.; Li, C.-L.; Li, R.; Zhang, J.; Ramakrishna, S.; Long, Y.-Z. Rotation-mode liquid-solid triboelectric nanogenerator for efficient contact-electro-catalysis and adsorption. Nano Energy 2023, 110, No. 108329.

(16) Chen, Z.; Lu, Y.; Liu, X.; Li, J.; Liu, Q. Novel magnetic catalysts for organic pollutant degradation via contact electro-catalysis. Nano Energy 2023, 108, No. 108198.

(17) Zhang, Y.; Zhao, J.; Zhang, L.; Zhao, Y.; Zhang, Y.; Cheng, L.; Wang, D.; Liu, C.; Zhang, M.; Fan, K.; Zhang, M. A cascade nanoreactor for enhancing sonodynamic therapy on colorectal cancer via synergistic ROS augment and autophagy blockage. *Nano Today* **2023**, *49*, No. 101798.

(18) Kang, J. S.; Jeong, H.; Jeong, M.; Kim, J.; Park, S.; Jung, J. Y.; An, J. M.; Kim, D. In situ activatable nitrobenzene-cysteine-copper (II) nano-complexes for programmed photodynamic cancer therapy. *J. Am. Chem. Soc.* **2023**, *145*, 27587−27600.

(19) Li, H.; Liu, Y.; Huang, B.; Zhang, C.; Wang, Z.; She, W.; Liu, Y.; Jiang, P. Highly efficient GSH-responsive "off-on" NIR-II fluorescent Fenton nanocatalyst for multimodal imaging-guided photothermal/chemodynamic synergistic cancer therapy. *Anal. Chem.* **2022**, *94*, 10470−10478.

(20) Son, S.; Kim, J. H.; Wang, X.; Zhang, C.; Yoon, S. A.; Shin, J.; Sharma, A.; Lee, M. H.; Cheng, L.; Wu, J.; Kim, J. S. Multifunctional sonosensitizers in sonodynamic cancer therapy. *Chem. Soc. Rev.* **2020**, *49*, 3244−3261.

(21) Li, Z.; Zhou, Z.; Wang, Y.; Wang, J.; Zhou, L.; Cheng, H.-B.; Yoon, J. Activatable nano-photosensitizers for precise photodynamic cancer therapy. *Coord. Chem. Rev.* **2023**, *493*, No. 215324.

(22) Wang, Z.; Li, H.; She, W.; Zhang, X.; Liu, Y.; Liu, Y.; Jiang, P. 3-Bromopyruvate-loaded Ti_3C_2 MXene/Cu_2O nanosheets for photo-acoustic imaging-guided and hypoxia-relieving enhanced photo-thermal/chemodynamic therapy. *Anal. Chem.* **2023**, *95*, 1710−1720.

(23) Cen, D.; Zheng, Q.; Zheng, B.; Zhou, R.; Xiao, X.; Zhang, T.; Huang, Z.; Yan, T.; Yu, J.; Li, X.; Deng, R.; Cai, X. A near-infrared light-responsive ROS cascade nanoplatform for synergistic therapy potentiating antitumor immune responses. *Adv. Funct. Mater.* **2023**, *33*, No. 2211402.

(24) Song, X.; Feng, L.; Liang, C.; Yang, K.; Liu, Z. Ultrasound triggered tumor oxygenation with oxygen-shuttle nanoperfluorocarbon to overcome hypoxia-associated resistance in cancer therapies. *Nano Lett.* **2016**, *16*, 6145−6153.

(25) Riesz, P.; Kondo, T. Free radical formation induced by ultrasound and its biological implications. *Free Radical Biol. Med.* **1992**, *13*, 247.

(26) Jiang, P.; Zhang, L.; Guo, H.; Chen, C.; Wu, C.; Zhang, S.; Wang, Z. L. Signal output of triboelectric nanogenerator at oil-water-solid multiphase interfaces and its application for dual-signal chemical sensing. *Adv. Mater.* **2019**, *31*, No. e1902793.

(27) Loh, Z. H.; Doumy, G.; Arnold, C.; Kjellsson, L.; Southworth, S. H.; Al Haddad, A.; Kumagai, Y.; Tu, M. F.; Ho, P. J.; March, A. M.; Schaller, R. D.; Yusof, M. S. B.; Debnath, T.; Simon, M.; Welsch, R.; Inhester, L.; Khalili, K.; Nanda, K.; Krylov, A. I.; Moeller, S.; Coslovich, G.; Koralek, J.; Minitti, M. P.; Schlotter, W. F.; Rubensson, J. E.; Santra, R.; Young, L. Observation of the fastest chemical processes in the radiolysis of water. *Science* **2020**, *367*, 179−182.

(28) Zhang, Y.; Zhang, X.; Yang, H.; Yu, L.; Xu, Y.; Sharma, A.; Yin, P.; Li, X.; Kim, J. S.; Sun, Y. Advanced biotechnology-assisted precise sonodynamic therapy. *Chem. Soc. Rev.* **2021**, *50*, 11227−11248.

(29) Bai, S.; Yang, N.; Wang, X.; Gong, F.; Dong, Z.; Gong, Y.; Liu, Z.; Cheng, L. Ultrasmall iron-doped titanium oxide nanodots for enhanced sonodynamic and chemodynamic cancer therapy. *ACS Nano* **2020**, *14*, 15119−15130.

(30) Li, H.; Yang, X.; Wang, Z.; She, W.; Liu, Y.; Huang, L.; Jiang, P. A near-infrared-II fluorescent nanocatalyst for enhanced CAR T cell therapy against solid tumor by immune reprogramming. *ACS Nano* **2023**, *17*, 11749−11763.

(31) Pan, Y.; Xu, C.; Deng, H.; You, Q.; Zhao, C.; Li, Y.; Gao, Q.; Akakuru, O. U.; Li, J.; Zhang, J.; Wu, A.; Chen, X. Localized NIR-II laser mediated chemodynamic therapy of glioblastoma. *Nano Today* **2022**, *43*, No. 101435.

(32) Liu, Y.; Zhao, Y.; Li, H.; Zhang, X.; Wang, Z.; She, W.; Jiang, F.; Liu, Y.; Jiang, P. Dual-targeting and multimodal imaging-guided photothermal/chemodynamic synergistic therapy boosted by ascorbic acid-induced H_2O_2 in situ self-supply. *ACS Appl. Mater. Interfaces* **2023**, *15*, 9841−9852.

(33) Yin, Y.; Jiang, X.; Sun, L.; Li, H.; Su, C.; Zhang, Y.; Xu, G.; Li, X.; Zhao, C.; Chen, Y.; Xu, H.; Zhang, K. Continuous inertial cavitation evokes massive ROS for reinforcing sonodynamic therapy and immunogenic cell death against breast carcinoma. *Nano Today* **2021**, *36*, No. 101009.

(34) Xie, W.; Chen, B.; Wen, H.; Xiao, P.; Wang, L.; Liu, W.; Wang, D.; Tang, B. Z. Biomimetic nanoplatform loading Type I aggregation-induced emission photosensitizer and glutamine blockade to regulate nutrient partitioning for enhancing antitumor immunotherapy. *ACS Nano* **2022**, *16*, 10742−10753.

(35) Li, H.; Chen, C.; Wang, Z.; Huang, Y.; He, G.; Liu, Y.; Jiang, P.; Wang, Z. L. Triboelectric immunotherapy using electrostatic-break-down induced direct-current. *Mater. Today* **2023**, *64*, 40−51.

(36) Wei, B.; Pan, J.; Yuan, R.; Shao, B.; Wang, Y.; Guo, X.; Zhou, S. Polarization of tumor-associated macrophages by nanoparticle-loaded *Escherichia coli* combined with immunogenic cell death for cancer immunotherapy. *Nano Lett.* **2021**, *21*, 4231−4240.

(37) Ji, G.; Zhang, Y.; Si, X.; Yao, H.; Ma, S.; Xu, Y.; Zhao, J.; Ma, C.; He, C.; Tang, Z.; Fang, X.; Song, W.; Chen, X. Biopolymer immune implants' sequential activation of innate and adaptive immunity for colorectal cancer postoperative immunotherapy. *Adv. Mater.* **2021**, *33*, No. e2004559.

(38) Zhou, Y.; Guo, Y.; Chen, L.; Zhang, X.; Wu, W.; Yang, Z.; Li, X.; Wang, Y.; Hu, Z.; Wang, Z. Co-delivery of phagocytosis checkpoint and STING agonist by a Trojan horse nanocapsule for orthotopic glioma immunotherapy. *Theranostics* **2022**, *12*, 5488−5503.

(39) Wu, W.; Pu, Y.; Yao, H.; Lin, H.; Shi, J. Microbiotic nanomedicine for tumor-specific chemotherapy-synergized innate/adaptive antitumor immunity. *Nano Today* **2022**, *42*, No. 101377.

(40) Cheng, Y.; Pu, X.; Liu, M.; Kuang, S.; Zhang, P.; Hua, Q.; Cong, Z.; Guo, W.; Hu, W.; Wang, Z. L. Perfluorocarbon nanoparticles enhance reactive oxygen levels and tumour growth inhibition in photodynamic therapy. *Nat. Commun.* **2015**, *6*, No. 8785.

(41) Yang, Z.; Luo, Y.; Yu, H.; Liang, K.; Wang, M.; Wang, Q.; Yin, B.; Chen, H. Reshaping the tumor immune microenvironment based on a light-activated nanoplatform for efficient cancer therapy. *Adv. Mater.* **2022**, *34*, No. e2108908.

(42) Luo, G.; Li, X.; Lin, J.; Ge, G.; Fang, J.; Song, W.; Xiao, G. G.; Zhang, B.; Peng, X.; Duo, Y.; Tang, B. Z. Multifunctional calcium-manganese nanomodulator provides antitumor treatment and improved immunotherapy via reprogramming of the tumor micro-environment. *ACS Nano* **2023**, *17*, 15449−15465.

(43) Nie, C.; Pan, W.; Wu, B.; Luo, T.; Lv, J.; Fan, Y.; Feng, J.; Liu, C.; Guo, J.; Li, B.; Bai, X.; Zheng, L. Engineered enzyme-loaded erythrocyte vesicles precisely deprive tumoral nutrients to induce synergistic near-infrared-II photothermal therapy and immune activation. *ACS Nano* **2023**, *17*, 13211−13223.

(44) Zhang, J.; Huang, D.; Saw, P. E.; Song, E. Turning cold tumors hot: from molecular mechanisms to clinical applications. *Trends Immunol.* **2022**, *43*, 523−545.

(45) Yang, L.; Zhang, Y.; Zhang, Y.; Xu, Y.; Li, Y.; Xie, Z.; Wang, H.; Lin, Y.; Lin, Q.; Gong, T.; Sun, X.; Zhang, Z.; Zhang, L. Live macrophage-delivered doxorubicin-loaded liposomes effectively treat triple-negative breast cancer. *ACS Nano* **2022**, *16*, 9799−9809.

(46) Zhang, Y.; Xu, J.; Fei, Z.; Dai, H.; Fan, Q.; Yang, Q.; Chen, Y.; Wang, B.; Wang, C. 3D printing scaffold vaccine for antitumor immunity. *Adv. Mater.* **2021**, *33*, No. e2106768.

(47) Chen, H.; Liu, L.; Ma, A.; Yin, T.; Chen, Z.; Liang, R.; Qiu, Y.; Zheng, M.; Cai, L. Noninvasively immunogenic sonodynamic therapy with manganese protoporphyrin liposomes against triple-negative breast cancer. *Biomaterials* **2021**, *269*, No. 120639.

(48) Yue, J.; Mei, Q.; Wang, P.; Miao, P.; Dong, W. F.; Li, L. Light-triggered multifunctional nanoplatform for efficient cancer photo-immunotherapy. *J. Nanobiotechnol.* **2022**, *20*, No. 181.